Analysis of the Airfoil Stall With a Modification of Viscous-Inviscid Interaction Concept

E. L. Amromin
Mechmath LLC,
Prior Lake, MN 55372

A modification of the viscous-inviscid interaction concept with the employment of coupled vortices around the airfoil wake is introduced for analyzing the airfoil stall. The analyzed flow includes the laminar boundary layers, laminar separation bubble, laminar-turbulent transition zone, turbulent boundary layers, turbulent separation zone, wake, and outer inviscid flow. Integral methods are employed for the boundary layers. The boundaries of separation zones are analyzed as free surfaces, however, their lengths and shapes depend on the Reynolds number. The described modification is validated by a comparison of the numerical results with the previously published experimental data for various airfoils and Reynolds numbers at low Mach numbers. This modification achieves a reasonably good agreement of the computed lift and moment coefficients with their measured values.
[DOI: 10.1115/1.4023784]

1 Introduction

With all of the recent successes of computational fluid dynamics (CFD), the analysis of the airfoil stall remains a challenge. Reynolds-averaged Navier–Stokes (RANS) codes and other computational tools considering "fully turbulent" flows represent the contemporary CFD mainstream. However, it is a challenge for these tools to correctly predict the maximum airfoil lift and its decrease caused by a further increase of the angle of attack, as shown in Fig. 1, with typical examples of the computations carried out by Maughmer and Coder [1] with various codes of various developers for a set of airfoils.

One can see that the RANS code OVERFLOW overestimates the maximum lift value, the RANS code FLUENT gets this maximum (at $\mathrm{Re} = 3 \times 10^5$ that should not correspond to a fully turbulent flow) but cannot run for higher angles of attack, and the viscous-inviscid interaction concept (VIIC) code PROFIL07 with integral methods for boundary layers without an analysis of their separation zones also cannot. (Let us recall that in VIIC, the flow is divided into viscous and inviscid parts with the interaction based on two effects: the pressure gradient influences the thicknesses of the boundary layers and wakes, but these thicknesses influence the pressure itself.) As shown in Fig. 2 with data from Martin et al. [2], there is also a substantial difference between the pressure predicted by the RANS code and the measured pressure distributions. The biggest difference takes place near the foil leading edge, where laminar separation occurs in the real flow. Such a situation with models of fully turbulent flows is explicable because, as emphasized in the recent review by Raiesi et al. [3], all contemporary turbulence models were tuned to specific data sets for attached turbulent flows at high-Reynolds numbers. These models should not run well for complex separated flows with a laminar boundary layer and laminar separation at the leading edge and with large turbulent separation at the trailing edge.

Alternatively, the VIIC methods allow for the analysis of multizone flows with laminar boundary layers and the transition of separated, reattached, and boundary layers (as computed by Kwon and Pletcher [4,5]). The VIIC also allows for the analysis of boundary layer separation behind bodies (as computed by Arndt et al. [6]). Nevertheless, a successful example of the use of the VIIC for airfoil stall has not yet been presented.

The first stall peculiarity is in the existence of a separation zone covering the foil trailing edge. This zone is approximately a constant pressure zone. Second, the pressure on the upper and lower sides of the wake downstream of this zone must be equal. These two peculiarities complicate the pressure computation (that must be found by solving an ideal fluid theory problem in the VIIC). Thus, it is useful to look for a similar purely ideal fluid theory problem. The problem of foil supercavitation is such a problem because it also includes a constant pressure zone behind a foil and the unloaded wake downstream of this zone. Recently, Fridman and Achkinadze [7] described the solution of this ideal fluid theory problem with the use of the half-century old scheme invented by Tulin [8] (shown in the upper part of Fig. 3). The combination of the two aforementioned conditions was satisfied in Refs. [7,8] with the employment of two spiral vortices of an opposite intensity located at different sides of the constant pressure zone. As is also shown in Ref. [7], solutions for the ideal fluid flow with constant pressure zones behind the foil at some angle of attack can be obtained without these vortices, but it is impossible to obtain the unloaded wake without them.

It is difficult to use the method [7] with its conformal mapping for stall computation. Successfully applied to plates, wedges, and other polygonal contours, this method does not work well for foils because of the difficulty to find the foil image in any hodograph plane, but the analysis [7,8] was very useful because it allows for two important conclusions:

- The combination of the two aforementioned conditions can be satisfied only with the employment of a pair of vortices of opposite intensity.
- Such an ideal fluid problem has multiple solutions because two parameters (for example, the abscissas of these vortices) are undetermined and must be either ordered or found from some additional conditions.

The suggested separated flow scheme (shown in the lower part of Fig. 3) does not copy the Tulin scheme, but it is rather his scheme modification for the foil stall analysis with the use of the VIIC. Two vortices are not placed just on the streamlines going from the foil surface, but they are placed at both sides of the foil wake. The vortex location quantitatively fits many stall

Manuscript received January 11, 2012; final manuscript received February 7, 2013; published online April 8, 2013. Assoc. Editor: Meng Wang.

 Copyright © 2013 by ASME

Downloaded From: https://fluidsengineering.asmedigitalcollection.asme.org on 07/02/2019 Terms of Use: http://www.asme.org/about-asme/terms-of-use

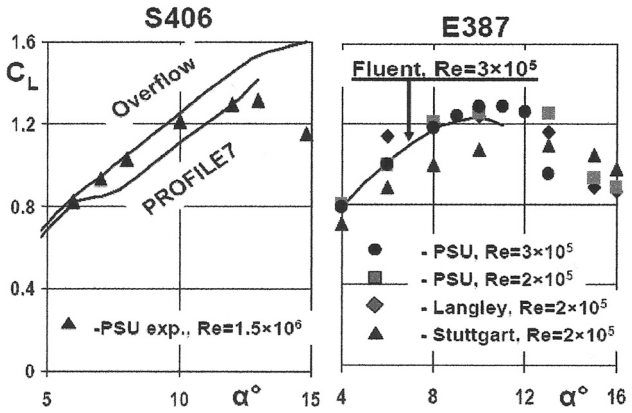

Fig. 1 Comparison of the lift and drag prediction with the RANS codes (OVERFLOW and FLUENT) and the viscous-inviscid interaction code (PROFIL07) with the experimental data for airfoils S406 and E387

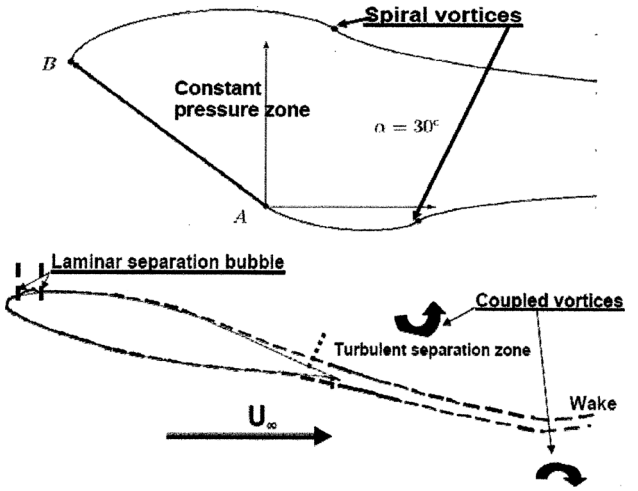

Fig. 3 Foil separated flows. (top) Flow around the plate with a constant pressure zone behind it, computed using the Tulin scheme with coupled spiral vortices. (bottom) Suggested scheme of the foil separated flow. The solid line is the foil contour; the dashed line is the computed section of the displacement body surface *S* that is the effective boundary of the outer inviscid flow. The dotted line shows the upper section of the turbulent separation zone.

visualizations (starting from that provided by Batchelor [9] in his photo 5.11.1b).

The description of the flow scheme and the corresponding numerical methods (including the effect of changes of the vortex location) is given here in more detail. This description is supplemented by a comparison of computational results for two-dimensional flows with experimental data for low M.

2 Flow Scheme and Numerical Method

The main results of the foil stall analysis are lift, moment, and drag values. The forces on the foil are mainly predetermined by the pressure in the surrounding inviscid flow (though the pressure normal derivative may be not small at some foil parts). However, the boundary between the inviscid flow and shear layers surrounding the foil depends on Re and initially are unknown. Because of the existence of an unknown boundary, the problem is nonlinear.

Furthermore, because of the boundary dependency on Re, the determination of shear layers inside this boundary must be made with regard to the variation of the right-hand side of the momentum equation with the variation of Re. For airfoils at high angles of attack the shear layers generally include diverse zones (the laminar boundary layer, separation bubble, attached turbulent boundary layer, turbulent separation zone, and wake) and this right-hand side substantially varies from one zone to another. This variety is a big challenge because numerous empirical coefficients are necessary to describe each zone. This necessity is inherent to the large eddy simulation (LES) and RANS methods (even the simplest RANS Spalart–Allmaras model for attached flows uses at least 17 empirical and tuning coefficients) and to integral

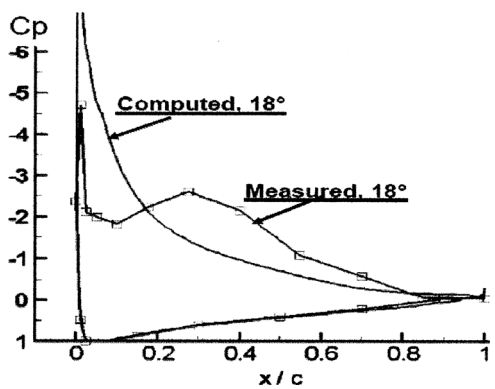

Fig. 2 Measured [2] and computed results with a RANS code pressure coefficient *Cp* on the airfoil at $\alpha = 18^\circ$ and M = 0.3

boundary layer methods (that use less empirical coefficients, but sacrifice a possibility to describe the flow in more detail due to the preliminary integration of mass conservation and momentum equations across the layers). The criteria of determination of the boundaries between zones are usually derived from the similarity analysis that also requires empirical inputs.

Thus, a multizone analysis is the necessity, whereas the rationale of the use of integral methods is in the simplicity allowing for easier estimation of the most important parameters without a detriment to the stability of the whole computational algorithm. A further combined use of the VIIC with RANS is also possible (such examples were described, in particular, by Larsson et al. [10]).

There are several steps to solving this problem. The first step consists of the determination of the inviscid flow around the foil. This step provides the pressure distribution along the foil contour. The second step consists of the determination of the foil boundary layer characteristics. Separation bubbles are possible there. Because the location and sizes of these bubbles are not known *a priori*, iterations are required in the bubble analysis. Any iteration is based on solving the linear equations with coefficients fitted from iteration to iteration. Thus, quasi-linearization of the problem is used. The third step consists of the iterative determination of the shape of the wake and turbulent separation zone covering the foil trailing edge. Quasi-linearization is also used for this step.

The inviscid flow around the foil can be determined by solving a boundary value problem for the Laplace equation for the velocity potential $\Phi(x, y, Q, \Gamma)$

$$\Delta\Phi = 0 \tag{1}$$

In addition to Eq. (1) there is the boundary condition on the normal velocity, written as

$$\partial\Phi/\partial N|_S = 0 \tag{2}$$

and the incoming flow definition $\text{grad}\,\Phi|_{x=\pm\infty} = \{\cos\alpha, \sin\alpha\}$. Equations (1) and (2) can be solved using an integral equation of potential theory when an additional condition for the lift/velocity circulation is defined. Traditionally, it has been the Kutta–Joukowski condition, however, this condition does not work for foils with separated zones behind trailing edges. On the contrary, this zone can be considered as a constant pressure zone.

Downloaded From: https://fluidsengineering.asmedigitalcollection.asme.org on 07/02/2019 Terms of Use: http://www.asme.org/about-asme/terms-of-use

As explained in Ref. [6], the consequence of this constancy for a time-independent flow is the condition

$$\int_{x_{1up}}^{x_R} \frac{U(\xi, y_u)d\xi}{\sqrt{(\xi - x_{1up})(x_R - \xi)}} = -\int_{x_{1LO}}^{x_R} \frac{U(\xi, y_l)d\xi}{\sqrt{(\xi - x_{1LO})(x_R - \xi)}} \quad (3)$$

Behind this zone (at $x_R < x < X_W$) a medium part of the wake is located. This part must be unloaded, at least integrally

$$\int_{x_R}^{X_W} U(\xi, y_u)d\xi = -\int_{x_R}^{X_W} U(\xi, y_l)d\xi \quad (4)$$

For $x > X_W$ a far wake parallel to the incoming flow is located. Here, $|U| = 1.0$ at this part of the wake, thus, its contribution to the derivatives of Φ can be calculated with simple formulas. Solving Eqs. (1)–(4) makes it possible to determine the lift coefficient (or Γ) together with the intensity Γ^* of the coupled vortices.

For the boundary layer analysis, the integral methods are employed. As recommended by Cebici and Bradshaw [11], the Falkner–Scan profile is used in the laminar boundary layer and the laminar-turbulent transition is predicted with the semiempirical Michel criterion (as was noted by W. Rodi, this criterion is the most accurate for flows with adverse pressure gradients). Laminar separation can occur when $H^* > 4.0$ and then the boundary layer becomes turbulent in the bubble itself.

The turbulent boundary layer analysis is based on solving the integral momentum equation and the mass conservation equation for this layer. Let us consider the simplest case of a shear layer in a two-dimensional incompressible flow along a surface of a small curvature. The momentum differential equation for a turbulent layer can be then rewritten in Cartesian variables, from Townsend [12]

$$\frac{\partial u}{\partial t} + \frac{\partial}{\partial x}\left(u^2 + \left\langle u'^2 \right\rangle - \left\langle v'^2 \right\rangle + \frac{P}{\rho}\right) + \frac{\partial}{\partial y}\left(uv + \langle u'v' \rangle - \mu\frac{\partial u}{\partial y}\right) = 0$$

Here, P relates to the layer boundary. The general technique used to derive integral equations can be applied to this layer. Let us consider only steady flows. Integration across the layer transforms the preceding differential equation into a modified two-dimensional Karman equation

$$\frac{\partial \delta^{**}}{\partial x} + \frac{\delta^{**}}{U}\left(2 + \frac{\delta^*}{\delta^{**} - \delta^P}\right)\frac{\partial U}{\partial x} = \frac{C_f}{2} + \left(\frac{\delta^{**}}{1 - \delta^P/\delta^{**}}\right)\frac{\partial}{\partial x}\left(\frac{\delta^P}{\delta^{**}}\right) \quad (5)$$

The integral mass conservation law is used as the second equation

$$d(U\delta^*)/dx = d(U\delta)/dx - V^* \quad (6)$$

In the attached turbulent boundary layer the approximation $V^* = 0.0306[(\delta - \delta^*)/\delta^{**} - 3]^{-0.617}$ of the normal velocity component (recommended by Cebici and Bradshaw [11]) is used.

It is necessary to select the velocity profiles $u(y/\delta)/U$ and approximations of the right-hand sides of Eqs. (5) and (6) for their integration. Diverse selections were made for the attached and separated boundary layers. The traditional velocity profile $u(y) = f(y) + [U - f(\delta)]F(y,0,\delta,\varepsilon)$ with $\varepsilon = 3$, $f(y) = v^*[\ln(yv^*/\nu)/\kappa + B^*]$ and $C_f = 2v^{*2}$ is used for the attached turbulent boundary layer, whereas δ^P is neglected there. Thus, two parameters $\{v^*, \delta\}$ in this velocity profile are used in Eqs. (5) and (6) for such a layer.

The momentum equation for the separation bubble has the same form (the separation zone sketch is shown in Fig. 4 for the flow behind a backward step as the simplest typical example of separation with the boundary layer reattachment). However, there is no logarithmic sub-layer in separated flows, as proven by Agarwal and Simpson [13]. In accordance with their data, the velocity profile is selected as $u(y) = [U - u_p]F(y, Y, \delta, \varepsilon) + u_p$ at $\varsigma \equiv y/Y \geq 1$ and $u = (1.3 - 0.3\zeta + 0.3\ln|\zeta|)$ at $\varsigma \leq 1$; $Y = 0.3u_P C/U$. Thus, two parameters of the velocity profile in the separated bubble are $\{\delta, u_p\}$. The second term in the right-hand side of Eq. (5) plays the significant role in separated layers and here $\delta^P = \beta\delta$ with β found from an approximation of the Eaton and Johnston [14] data. The direct consequence of the Prandtl formula for the turbulent stress $C_f = \gamma\kappa^2 u_P|u_P|$ with $\gamma = \text{const}$ is employed in Eq. (5).

The mass conservation law in the separation bubble is written using the exact formulation of the Prandtl's concept of the displacement body

$$\delta^*(x, u_P(x), \delta(x)) = T(x, U) \quad (7)$$

The initially unknown distance T implicitly depends on the tangent velocity U along the part of S over the separation bubble and must be tuned to U. The following form of the velocity U with undetermined coefficients is selected for the flow over the separation bubble with regard to the experimental data:

$$U = U_0 + U_1 F(x, 0, L/2, \varepsilon_1) + U_2 F(x, L/2, L + dL, \varepsilon_2) \quad (8)$$

Here, $\zeta = (x - a)/(b - a)$, ε_1, ε_2, and the ratio dL/L are approximation constants, however, the coefficients $U_0, U_1, U_2,$ and L implicitly depend on Re and must be found using the conditions of boundary layer separation and reattachment. As described by Amromin [15] for another case of incompressible flow with boundary layer separation and reattachment, these conditions are

$$\left.\frac{\delta^*}{U}\frac{dU}{dx}\right|_{x=L} = \sigma; \quad u_P(L) = 0; \quad \left.\frac{dT}{dx}\right|_{x=L+dL} < \infty; \quad \left.\frac{dU}{dx}\right|_{x=0} = \left.\frac{dU}{dx}\right|_{x=-0} \quad (9)$$

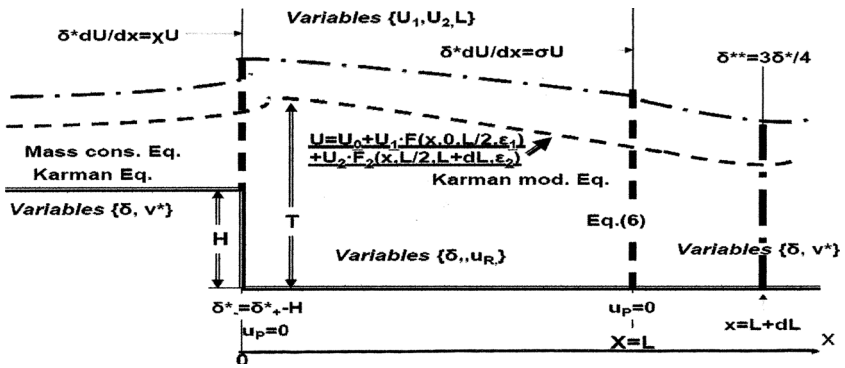

Fig. 4 Scheme of the separated flow behind a step: the dashed line is the displacement body section. The dash-dotted line is the boundary between the inviscid flow and the viscous flow.

Downloaded From: https://fluidsengineering.asmedigitalcollection.asme.org on 07/02/2019 Terms of Use: http://www.asme.org/about-asme/terms-of-use

The first of these conditions is the semiempirical reattachment criterion, whereas others are conditions of the flow continuity at the boundaries between zones.

The combined determination of U_0, U_1, U_2, T is performed with the problem quasi-linearization similar to that used in Refs. [6,16]. Small perturbations $\{h,q\}$ of the functions $\{T,Q\}$ are considered along the boundary of the separation zone. The perturbed Eqs. (8) and (2) can be rewritten as

$$\partial\Phi(x,y,q,0)/\partial\xi + \partial\Phi(x,y,Q,0)/\partial\xi = U \tag{10}$$

$$2\partial(hU)/\partial\xi = q \tag{11}$$

and solved with the subsequent correction of T. The integration of Eqs. (5) and (7) with the determined L, U, and T uses $\delta^*(0)$ and $u_P(0)$ as the initial data.

Furthermore, according to Ref. [3], an intermediate region just downstream of the separation bubble ($L < x < L + dL$) is the most difficult for modeling. There, the boundary layer restores the logarithmic velocity profile and the second term in the right-hand side of Eq. (5) is comparable with the first term due to unsteadiness of the real flow. Therefore, a special approximation for either H^* or δ^P is used. The computed $h(x)$ is used to correct the 'S' shape for the next iteration. The final accuracy of bubble computation is evaluated by substituting its solution in Eq. (8).

The reattached boundary layer at $x > L + dL$ will be computed with the same Eqs. (5) and (6). These computations go up to a point where the layer parameters yield the turbulent boundary layer separation criterion with a $\chi = \text{const}$

$$\delta^* dU/dX = \chi U \tag{12}$$

This point is the beginning of the turbulent separation zone covering the trailing edge and evolving into the wake. As shown by Castillo et al. [16], the beginning of the separation zone on a smooth wall (like airfoils) in 2D time-averaged flows is indicated by Eq. (12) with an acceptable accuracy.

Correction of the wake shape can be carried out with Eqs. (10) and (11). According to Eqs. (3) and (4) the wake shape depends on x_R, along with Γ^* and C_L. Thus, various solutions with various x_R are possible. To select the unique solution for the wake one can consider Eq. (5) in the simplified form

$$\frac{\delta^{**}(x_R)}{\delta^{**}(1)} = \left[\frac{U(1)}{U(x_R)}\right]^{2+0.5[H^*(1)+H^*(x_R)]} \tag{13}$$

It is easy to transform Eq. (13) into the well-known Squire–Young formula, assuming $H^*(x_R) = U(x_R) = 1$.

As an example of the coefficient tuning in the VIIC, the influence of dL/L on the computational results is shown in Fig. 5, in comparison with data by Tani et al. [17]. Information on the numerical accuracy (grid effect) of the used iterative algorithm was presented in [15]. Specifically, for the turbulent layers described by Eq. (5) the boundary layer grid effect was also analyzed. It was found that the region most sensitive to the grid size is the region of the boundary layer reattachment, but its breakdown into 45,000 cells allows for the less than 0.01% changes in δ^{**}.

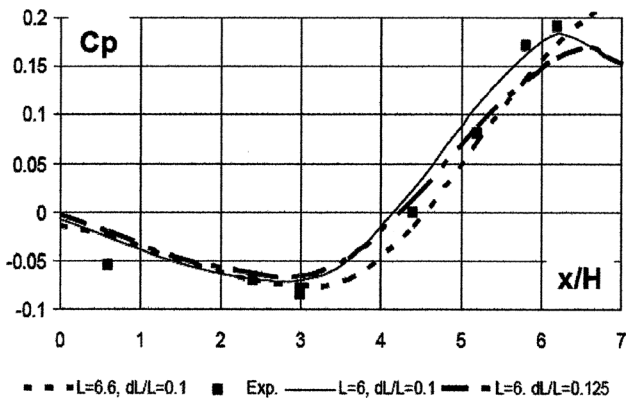

Fig. 5 Effect of *dL/L* on the computed pressure distribution in comparison with the experimental data [17]

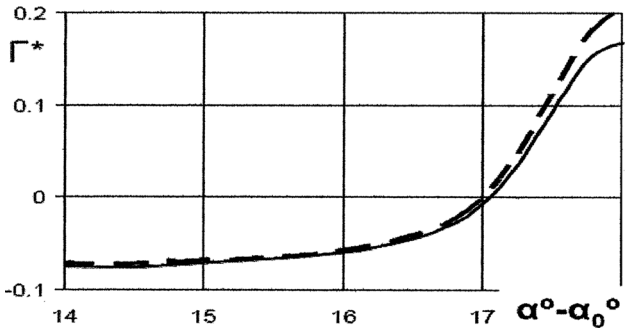

Fig. 6 Effect of the second vortex location on the intensity of the vortex pair behind the foil S805

The effect of the vortex pair location on the vortex pair intensity Γ^* is illustrated in Fig. 6 for the airfoil S805. In two compared variants, the first vortex was located just over the trailing edge. The abscissa of the second vortex was varied from $0.6(x_R - 1)C + C$ (the corresponding Γ^* is shown by the solid line) to $0.75(x_R - 1)C + C$ (the corresponding Γ^* is shown by the dashed line). For the same accuracy in yielding Eqs. (3) and (4), the values of x_R and C_L are slightly different for these variants (the difference in C_L is less than 0.01). It is interesting that Γ^* goes through zero approximately at the angle of attack of the maximum lift.

It is possible such "moderate nonuniqueness" of the problem solution reflects some instability of this separated flow. Possibly, the dependency of Γ^* on the vortex location reflects evolutions of the real vortices. However, such instability and evolutions cannot be analyzed in the framework of this time-independent problem.

3 Intermediate Examples as the Method Verification

While developing a numerical method for a complex airfoil flow, one must first look for the intermediate validation related to simpler flows. The separation bubble near the leading edge significantly influences the pressure on the airfoil suction side and the extension of the separation zone upstream of the trailing edge. However, as follows from a typical velocity distribution shown in Fig. 7, the separation bubble on a foil at $\text{Re} \geq 3 \times 10^6$ is quite short and the detailed measurements are very difficult. Nevertheless, a comparison of the numerical and experimental results for the separation zones with boundary layer reattachment behind

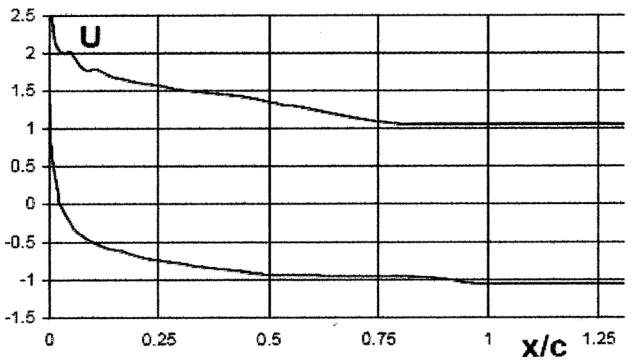

Fig. 7 Computed velocity along *S* for a NACA foil with the trailing edge separation at $\text{Re} = 3 \times 10^6$

Downloaded From: https://fluidsengineering.asmedigitalcollection.asme.org on 07/02/2019 Terms of Use: http://www.asme.org/about-asme/terms-of-use

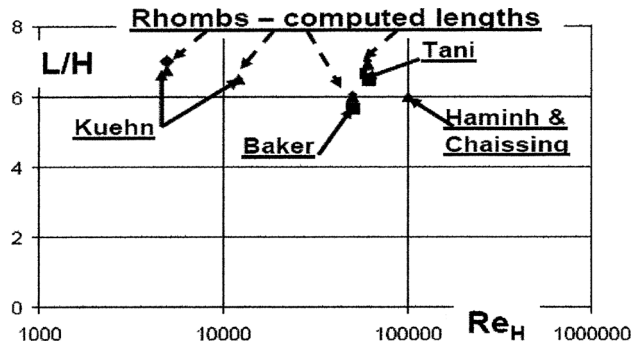

Fig. 8 Comparison of the computed and measured [14] length of the separation zones behind the backward steps

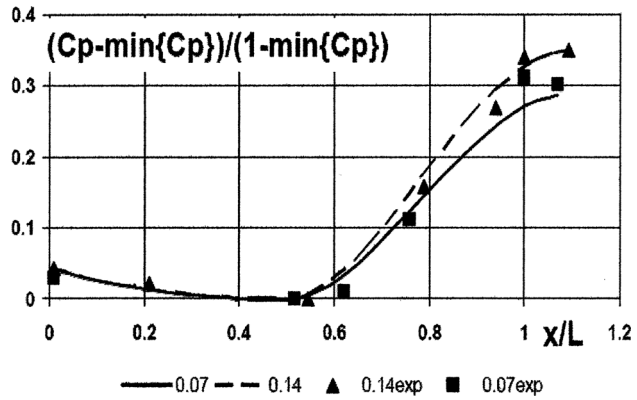

Fig. 9 Normalized pressure distribution: comparison between the presented computations and the experimental data [18] for separation zones behind the backward steps in channels. The numbers in the legend show the ratio of *H* to the channel width.

such zones is the most important intermediate validation. Fortunately, there is a rich data set for separation behind backward steps. The experimental data of Eaton and Johnston [14] and Ramamurthy et al. [18] for steps are used in the comparisons presented in Figs. 8 and 9. These data were employed in tuning the aforementioned coefficients and finally $\beta = 0.017$, $\varepsilon_1 = 1.2$, $\varepsilon_2 = 2$, $\sigma = -0.015$, and $\gamma = 1.25$ were selected. In the velocity profile for separation zones $\varepsilon = 1.25$.

Thus, one can see from the relatively simple flow examples in Figs. 8 and 9 that the selected velocity approximation along the separation bubble, the velocity profile within it, and the reattachment criteria (Eq. (9)) allows for a good computation of the separation bubble lengths and the pressure along them.

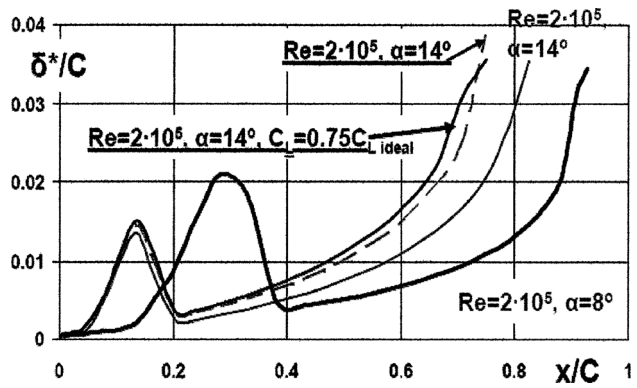

Fig. 10 Effects of the Reynolds number and angle of attack on the computed thickness displacement on NACA0021

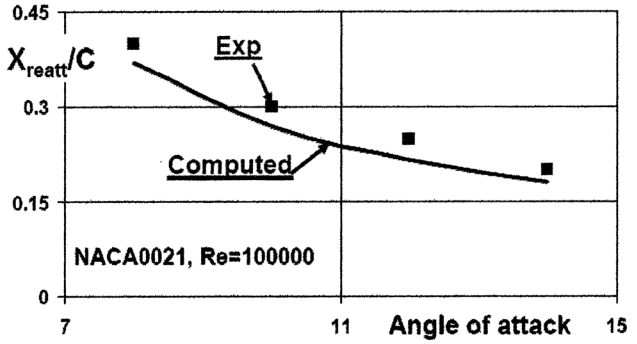

Fig. 11 Comparison of the computed and measured [19] points of the boundary layer reattachment behind a laminar bubble over the NACA0021

As is clear from Eq. (12), δ^* predetermines the location of the trailing edge separation considered as the wake beginning. One can see examples of the displacement thickness computed along the foil suction side with separation bubbles in Fig. 10. These results for low Re are more visible because of the larger bubble lengths.

Furthermore, reconstruction of the zone size by the measured pressure distribution is also a good implicit method, although it may be confident only for quite large L at quite small Re. Such reconstructions with the experimental data by Mabe et al. [19] with the NACA0021 airfoil at $\mathrm{Re} = 10^5$ are used in the comparisons of Fig. 11. Such indirect comparisons make it possible to evaluate the achieved agreement of the computations with the experimental data. As shown, this agreement is already satisfactory.

Nevertheless, let us point out that the goal of this work is to show the possibility of stall computation with the VIIC rather than to define the optimum sets of coefficients for such computations.

4 Analysis of Airfoil Stall

The computed foil lift and moment coefficients are compared here with the experimental data. The computed lift coefficients for various NACA airfoils tested by Mabe et al. [19] at very small M, by Beasley and McGhee [20] at $\mathrm{M} \approx 0.2$, and by McAlister et al. [21] at $\mathrm{M} = 0.3$ are compared with measurements in Figs. 12–14.

The proportionality of $dC_L/d\alpha$ to $1/\sqrt{1-M^2}$was taken into account in these computed dependencies (one may read, for example, Shapiro [22], for more detail). All referenced experiments have been carried out in restricted flows of wind tunnels. Though the tunnel walls increase C_L at fixed angles of attack, for the simplicity of the computations the unbounded flows were analyzed in

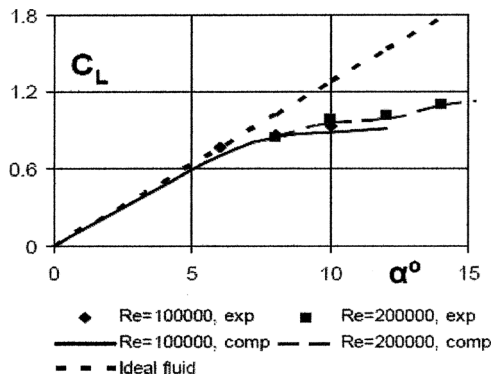

Fig. 12 Lift coefficient of the NACA 0021 airfoil; the curves show our computations and the symbols show the experimental data [19]

Downloaded From: https://fluidsengineering.asmedigitalcollection.asme.org on 07/02/2019 Terms of Use: http://www.asme.org/about-asme/terms-of-use

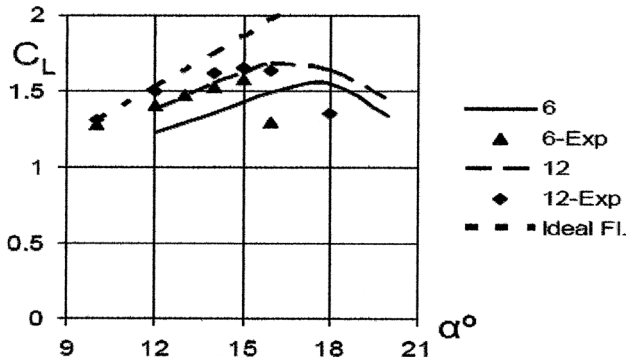

Fig. 13 Lift coefficient of the NACA651-213 a = 0.50 airfoil. The curves show the numerical results and the symbols show the experimental data [20]. The numbers in the legend show the values of Re/10^6.

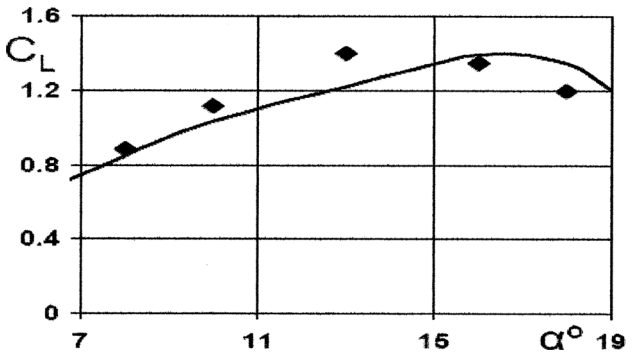

Fig. 14 Lift coefficient of the NACA0012 airfoil at Re = 3.9 × 10^6; the curve shows the numerical results and the symbols show the experimental data [21]

this paper. Nevertheless, the lift maxima themselves are well predicted for all considered airfoils and the decreases of $C_L(\alpha)$ after these maxima are satisfactorily predicted. Furthermore, the measured trends of the Re influence on C_L are correctly predicted (in Figs. 12 and 13): for a smaller Re, δ^* is greater and, in accordance with Eq. (12), the trailing edge separation occurs closer to the leading edge. This leads to a larger lift decrease (in comparison with the ideal fluid).

Although the computation [1] of the moment with OVERFLOW for stall conditions is even less accurate than the computation of the lift, the agreement of our computed moment coefficients with the experimental data in Fig. 15 is also satisfactory.

Application of the suggested method to non-NACA foils is illustrated in Fig. 16 with the experimental data by Silberstein

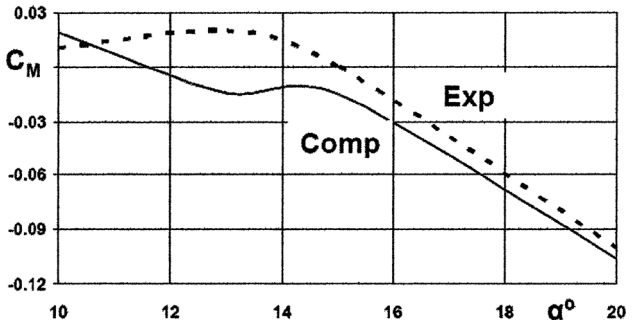

Fig. 15 Comparison between the computed and the experimental [21] moment coefficient of the airfoil NACA0012 at Re = 3.9 × 10^6

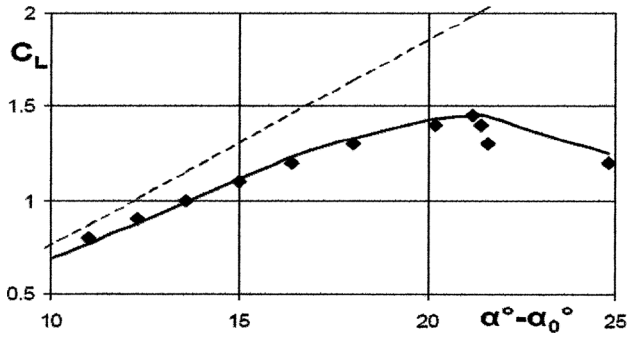

Fig. 16 Comparison between the computed (solid line) and measured [23] (rhombs) lift coefficient of the Clark-Y airfoil. At the highest lift Re = 4.2 × 10^6; Re rises to 4.8 × 10^6 at low lift. The dashed line shows the ideal fluid asymptote.

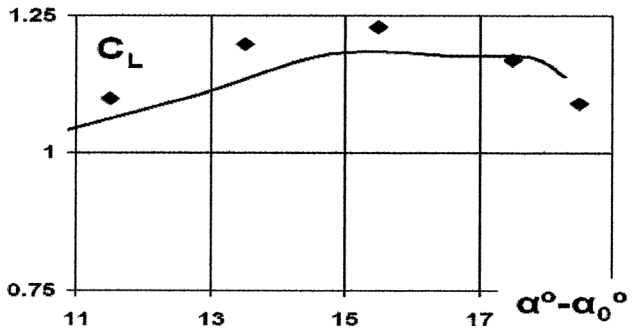

Fig. 17 Computed (solid line) and measured [1] (rhombs) lift coefficient of the S805 airfoil at Re = 10^6

[23] for the Clark airfoil and in Fig. 17 with data [1] for the S805 airfoil. For a more accurate comparison with the experimental data, the lift coefficients are compared at the same values of $\alpha^\circ - \alpha_0{}^\circ$. Although the computed lift decrease for the Clark airfoil does not start from a sharp drop, its difference with the measured lift is not large.

The goal of this paper is to manifest the possibilities offered by the described multizone concept, rather than to suggest its best implementation. Possibly, in the future it would be more accurate to use some differential methods for the determination of the viscous layers (as was already done in Ref. [4,5] for backward step flows) instead of the integral methods used here. In addition, extensions of the described analysis to a two-dimensional dynamic stall or a three-dimensional stall appear to be possible. Nevertheless, such extensions would require additional empirics for additional equations and more detailed descriptions of vortices (of tip vortices in three-dimensional flows and of drifting vortices in unsteady flows).

5 Conclusions

The numerical analysis of the stall remains to be an issue even for airfoils moving at a constant speed. The models of "fully turbulent" flows (now broadly employed in engineering) unsatisfactorily describe the airfoil stall. The suggested modification of the viscous-inviscid interaction concept employs a multizone model. This modification satisfactorily predicts the two-dimensional airfoil lift and moment at stall conditions, even with a very simplified modeling of the boundary layers (with the use of integral methods). Two main points of the stall analysis are emphasized:

1. A multi-zone analysis with taking into account the foil laminar boundary layer and its separation is necessary. It allows for a substantially better flow computation at stall

Downloaded From: https://fluidsengineering.asmedigitalcollection.asme.org on 07/02/2019 Terms of Use: http://www.asme.org/about-asme/terms-of-use

conditions. The advantage of the multizone approach for such complex flow overcomes the disadvantages of primitive integral methods used for shear flows here. Eventually, this approach could be enhanced by the use of the RANS or LES codes, at least in some zones

2. An account of the influence of large vortices located in the separation zone behind the trailing edge on the entire flow is necessary for a stall quantitative analysis. In the suggested VIIC method, this account is carried out in the framework of inviscid flow computation with a modification of the Tulin scheme with coupled vortices.

Nomenclature

B^* = parameter of logarithmic velocity profile
C = airfoil chord
C_f = friction coefficient
C_L = lift coefficient
$Cp = 2(P - P_\infty)/(\rho U_\infty{}^2)$ pressure coefficient
dL = length of reattachment zone behind separation bubble $F(y, a, \delta, \varepsilon) = (1 + \varepsilon)[(y - a)/\delta]^e - \varepsilon[(y - a)/\delta]^{e+1}$
h = perturbation of T
H = heights of the step
$H^* = \delta^*/\delta^{**}$
L = length of separation zone
M = Mach number
N = normal to S
P = pressure
P_∞ = unperturbed pressure
q = perturbation of Q
Q = intensity of source/sink distributed on S
Re = Reynolds number
S = boundary of inviscid flow
T = distance between foil surface and inviscid flow boundary
u, v = velocity components
u', v' = velocity pulsation components
u_P = maximum reverse velocity within a separation bubble
U = |grad(Φ)|
U_∞ = free stream speed
U_0, U_1, U_2 = coefficients in approximation of U along the separation bubble
v^* = friction velocity
V_N = normal velocity component on displacement body
$\{x,y,z\}$ = Cartesian coordinates
x_{1LO} = abscissa of separation at lower side of the trailing edge
x_{1up} = abscissa of separation at upper side of the trailing edge
x_R = abscissa of separation zone end behind the trailing edge
y = ordinate counted across the boundary layer
y_l = ordinate of the lower boundary of the wake
y_u = ordinate of the upper boundary of the wake
α = angle of attack
α° = angle of attack (in degrees)
$\alpha_0{}^\circ$ = angle of zero lift
β = factor in approximation of δ^P
γ = factor in the Prandtl formula for the turbulent stresses
Γ = intensity of vortices distributed along the foil chord
Γ^* = intensity of the vortex couple located in separation zone
δ = boundary layer thickness $\delta^P = U^{-2}\int_0^\delta(\langle u'^2\rangle - \langle v'^2\rangle)dy$
δ^* = displacement thickness
δ^{**} = momentum thickness
ε = coefficient in the velocity profile for separation bubble
$\varepsilon_1, \varepsilon_2$ = coefficients in U approximation along bubble
$\kappa \approx 0.4$ = von Karman constant
ν = kinematical viscosity
ρ = fluid density
σ = coefficient in boundary layer reattachment criterion
Φ = velocity potential
χ = coefficient in turbulent boundary layer separation criterion

References

[1] Maughmer, M. D., and Coder, J. G., 2010, "Comparisons of Theoretical Methods for Predicting Airfoil Aerodynamic Characteristics," U.S. Army Research, Development and Engineering Command Technical Report No. 10-D-106.
[2] Martin, P. B., McAlister, K. W., Chandrasekhara, M. S., and Geissler, W., 2003, "Dynamic Stall Measurements and Computations for a VR-12 Airfoil With a Variable Droop Leading Edge," American Helicopter Society 59th Annual Forum, Phoenix, AZ.
[3] Raiesi, H., Piomelli, U., and Pollard, A., 2011, "Evaluation of Turbulence Models Using Direct Numerical and Large-Eddy Simulation Data," ASME J. Fluids Eng., **133**(2), p. 021203.
[4] Kwon, O. K., and Pletcher, R. H., 1986, "A Viscous-Inviscid Interaction Procedure—Part 1: Method for Computing Two-Dimensional Incompressible Separated Channel Flows," ASME J. Fluids Eng., **108**(1), pp. 64–70.
[5] Kwon, O. K., and Pletcher, R. H., 1986, "A Viscous-Inviscid Interaction Procedure—Part 2: Application to Turbulent Flow Over a Rearward-Facing Step," ASME J. Fluids Eng., **108**(1), pp. 71–75.
[6] Arndt, R. E. A., Amromin, E. L., and Hambleton, W., 2009, "Cavitation Inception in the Wake of a Jet-Driven Body," ASME J. Fluids Eng., **131**(11), p. 111302.
[7] Fridman, G. M., and Achkinadze, A. S., 2001, "Review of Theoretical Approaches to Nonlinear Supercavitating Flows," NATO Applied Vehicle Technology Panel, Brussels, Report No. RTO EN-010.
[8] Tulin, M. P., 1964, "Supercavitating Flow—Small Perturbation Theory," J. Ship Res., **7**, pp. 16–37.
[9] Batchelor, G. K., 1970, *An Introduction to Fluids Dynamics*, Cambridge University Press, Cambridge, England.
[10] Larsson, L., Patel, V. C., and Dyne, G., 1991, "Ship Viscous Flow," SSPA, Gotenburg, Sweden, 1990 SSPA-CTN-IIHR Workshop Research Report.
[11] Cebeci, T., and Bradshaw, P., 1984, *Physical and Computational Aspects of Convective Head Transfer*, Springer-Verlag, New York.
[12] Townsend, A. A., 1976, *The Structure of Turbulent Boundary Layer*, Cambridge University Press, Cambridge, England.
[13] Agarwal, N. K., and Simpson, R. L., 1990, "Backflow Structure of Steady and Unsteady Separating Turbulent Boundary Layer," AIAA J., **28**, pp. 1764–1775.
[14] Eaton, J. K., and Johnston, J. P., 1981, "A Review of Research on Subsonic Turbulent Flow Reattachment," AIAA J., **19**, pp. 1093–1100.
[15] Amromin, E. L., 2002, "Scale Effect of Cavitation Inception on a 2D Eppler Hydrofoil," ASME J. Fluids Eng., **124**(1), pp. 186–193.
[16] Castillo, L., Wang, X., and George, W. K., 2004 "Separation Criterion for Turbulent Boundary Layers via Similarity Analysis," ASME J. Fluids Eng., **126**(3), pp. 297–304.
[17] Tani, I., Iuchi, M., and Komoda, H., 1961, "Experimental Investigation of Flow Separation Associated With a Step or a Groove," Aeronautical Research Institute, University of Tokyo, Report No. 364.
[18] Ramamurthy, A. S., Balanchandar, R., and Govinda Ram, H. S., 1991, "Some Characteristics of Flow Past Backward Facing Steps Including Cavitation Effects," ASME J. Fluids Eng., **113**(2), pp. 278–284.
[19] Mabe, J. H., Calkins, F. T., Wesley, B., Woszidlo, R., Taubert, L., and Wygnanski, I., 2007, "On the Use of Single Dielectric Barrier Discharge Plasma Actuators for Improving the Performance of Airfoils," AIAA Paper No. 3972.
[20] Beasley, W. D., and McGhee, R. J., 1975, "Experimental and Theoretical Low-Speed Aerodynamic Characteristics of the NACA 65_1-213, a = 0.5 Airfoil," NASA Technical Memorandum No. X-3160.
[21] McAlister, K. W., Pucci, S. L., McCroskey, W. J., and Carr, L. W., 1982, "An Experimental Study of Dynamic Stall on Advanced Airfoil Sections Volume. Pressure and Force Data," USA AVRADCOM Technical Report No. 82-A-8.
[22] Shapiro, A. H., 1953, *The Dynamics and Thermodynamics of Compressible Fluid Flow*, John Wiley and Sons, New York.
[23] Silberstein, A., 1935, "Scale Effect on Clark Y Airfoil Characteristics From NACA Full-Scale Wind Tunnel Tests," NACA Report No. 502.

Downloaded From: https://fluidsengineering.asmedigitalcollection.asme.org on 07/02/2019 Terms of Use: http://www.asme.org/about-asme/terms-of-use